Ag Nanoparticles on Reducible CeO 2 (111) Thin Films: Effect of Thickness and Stoichiometry of Ceria

8 AUTHORS, INCLUDING:

Yong Han
University of Science and Technology of China
16 PUBLICATIONS **100** CITATIONS

Qitang Fan
University of Science and Technology of China
13 PUBLICATIONS **93** CITATIONS

Junfa Zhu
University of Science and Technology of China
**122** PUBLICATIONS **1,238** CITATIONS

Ag Nanoparticles on Reducible CeO$_2$(111) Thin Films: Effect of Thickness and Stoichiometry of Ceria

Shanwei Hu, Yan Wang, Weijia Wang, Yong Han, Qitang Fan, Xuefei Feng, Qian Xu, and Junfa Zhu*

National Synchrotron Radiation Laboratory and Collaborative Innovation Center of Suzhou Nano Science and Technology, University of Science and Technology of China, Hefei, Anhui 230029, People's Republic of China

S *Supporting Information*

ABSTRACT: The growth and structures of Ag nanoparticles on CeO$_{2-x}$(111) thin films with different thicknesses, morphologies, and reduction degrees have been systematically studied by scanning tunneling microscopy (STM), X-ray photoelectron spectroscopy (XPS), and low energy electron diffraction (LEED). The CeO$_{2-x}$(111) thin films were epitaxially grown on Cu(111). With increasing the ceria thin film thickness, the size of the terraces decreases along with the increase of the number of open monolayers and defects. In most cases, Ag exhibits three-dimensional (3D) growth with constant particle densities on the CeO$_{2-x}$(111) surfaces at 300 K. Ag mainly populates the sites at the ceria–ceria step edges instead of ceria terraces, independent of the thicknesses but influenced by the reduction degree of the ceria films. On the fully oxidized ceria films, the particle density is directly proportional to the number of step edges of ceria, which is related to its thickness on Cu(111). On the slightly reduced ceria films which were prepared by annealing the fully oxidized ceria films in ultrahigh vacuum, single surface oxygen vacancies and their linear agglomerates are observed, but they do not anchor Ag particles during Ag deposition. While on the strongly reduced ceria films produced by decreasing the oxygen pressure during ceria film growth, large defect sites related to surface and subsurface oxygen vacancies are found; they can anchor the Ag nanoparticles, leading to the random distribution of Ag nanoparticles on ceria terraces upon deposition. Upon heating, the Ag nanoparticles undergo serious sintering before desorption at 800 K on the fully oxidized CeO$_2$ films. While on the reduced ceria films, the sintering and desorption processes are slowed down at the same annealing temperatures as those on CeO$_2$. This result suggests that the defects on reduced ceria surfaces can enhance the thermal stability of Ag nanoparticles during annealing.
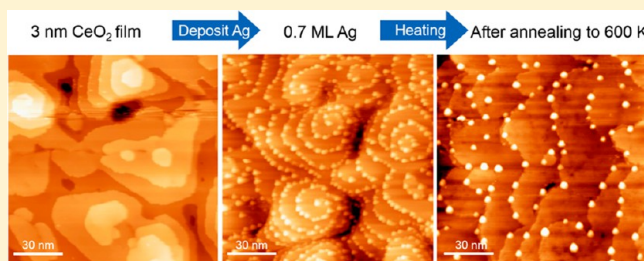
1. INTRODUCTION

Ceria (CeO$_2$ or nonstoichiometric CeO$_{2-x}$) is often served as an important support for metal catalysts which have been widely used in many chemical reactions, such as automotive exhaust treatment reactions, preferential oxidation of CO in the presence of H$_2$, water–gas shift reaction, steam reforming of oxygenates, and methane combustion.[1–6] In all these reactions, the catalytic properties of the catalysts benefit from the quick oxygen release/storage properties of ceria, which are basically due to the facile reversible transformation from the Ce^{4+} state to the Ce^{3+} state and the formation or annihilation of oxygen vacancies on the surface. To better understand the catalytic properties and the interaction of metal nanoparticles with the CeO$_2$ support, fundamental surface science studies in terms of the growth, structure, and reactivity of vapor-deposited metal nanoparticles on the CeO$_2$ surfaces are indispensable. However, bulk CeO$_2$ is an electrical insulating oxide which crystallizes in the fluorite structure with a band gap of 3.2–6.0 eV,[7] resulting in sample charge problem when using charged particles such as electrons or ions to probe the surface. To overcome this problem, single crystalline, well-defined CeO$_2$ thin films grown on metallic substrates are often employed as model systems in surface science studies. Various metals such as Pt,[8–10] Pd,[11]

Cu,[12,13] Rh,[11] Ag,[14–18] Au,[19–21] or Ni[22,23] deposited on thin CeO$_2$(111) model surfaces have been studied. It has been found that, in general, the late transition metal nanoparticles sintered more slowly or maintained smaller particles on ceria than on other metal oxide substrates.[24–26]

Among metal/ceria systems, Ag/CeO$_2$ is of particular interest because of its importance in technical applications as catalysts for many chemical reactions such as CO and hydrocarbon oxidation.[27] However, there are still some fundamental discrepancies remained, such as the oxidation state of Ag species and the mechanism of Ag-induced the reduction of CeO$_2$.[15,18] In a previous study, we reported the growth, electronic structure, and thermal stability of Ag on a 4 nm thick CeO$_2$(111) thin film grown on Ru(0001).[18] It was found that Ag grew three-dimensionally (3D) on CeO$_2$(111) with a constant particle density. The number of particle density was related to the surface roughness. By employing the Auger parameter method introduced by Wagner,[28] the contribution from the initial- and final-state effects to the binding energy

(BE) shifts of Ag $3d_{5/2}$ as a function of Ag coverages was discriminated; the BE shifts at low coverages were mainly attributed to the final-state (screening and relaxation) effects. Ag maintained metallic state on CeO_2. The reduction of CeO_2 upon Ag deposition was found, which was attributed to the spillover of oxygen from ceria to Ag at the Ag/CeO_2 boundary. Similar explanation for the reduction of ceria upon metal deposition has been made on Pt/CeO_2 by Libuda et al.[29] However, Luches et al. reported a different mechanism by investigating the same model system with combined experimental and theoretical studies.[15] They attributed the reason for the reduction of ceria induced by Ag deposition to the charge transfer from Ag to ceria. Their theoretical calculation results showed that the energy cost to create an oxygen vacancy from the regular $CeO_2(111)$ surface was too high, which made the transfer of oxygen from the ceria support to Ag particles energetically unfavorable. However, the situation for Ag growth on CeO_2 is different because in most cases the Ag atoms populate the defect sites. Therefore, it is expected that the energy cost to create an oxygen vacancy at a defect (step or kink) site should be different from the regular terrace site. In addition, the studies by Farmer et al. using microcalorimetry showed that the adsorption behavior of Ag on a 1 nm thick $CeO_{2-x}(111)$ film on $Pt(111)$ greatly differ from that on thicker films (>2 nm).[16,17] In order to gain a comprehensive understanding of the Ag/CeO_2 system, in this study we report a detailed STM study in combination with low-energy electron diffraction (LEED) and X-ray photoelectron spectroscopy (XPS) on the growth and thermal stability of Ag on ceria with different thicknesses and stoichiometries. It is found that Ag particles mainly populate the ceria–ceria step edges. The ceria films with different thicknesses show quite different morphologies, which induces different adsorption behavior of Ag nanoparticles. In addition, we have found that on the reduced ceria surfaces the reduction degree and the type of oxygen vacancies significantly affect the growth of Ag on ceria.

This paper is organized as following: After an introduction of experimental details, we report the detailed study of the growth of ordered ceria films on $Cu(111)$. Then the STM studies on the Ag deposition on ceria with different thickness and stoichiometry are presented, followed by giving the results of the thermal stabilities of Ag nanoparticles on stoichiometric and nonstoichiometric ceria surfaces. Finally, the influence of surface defects on Ag growth and sintering as well as the mechanism of Ag-induced ceria reduction are discussed.

2. EXPERIMENTAL SECTION

The experiments were performed in an ultrahigh vacuum (UHV) multichamber system which has been described in detail elsewhere.[30] Briefly, the system has capabilities to perform XPS/UPS, LEED, STM, and temperature-programmed desorption (TPD) experiments and consists of three chambers (analysis chamber, preparation chamber connected with a load lock, and variable-temperature Specs STM chamber) whose base pressures are all less than 2×10^{-10} Torr.

The $Cu(111)$ single crystal (8 mm diameter and 2 mm thick, from Mateck GmbH, Germany) was clamped to a Mo sample holder and heated through a combination of resistive heating and electron bombardment. A K-type thermocouple spot-welded to the edge of the sample holder was used to monitor the temperature. The true sample temperature has been calibrated by a separate experiment where a second K-type

thermocouple was directly spot-welded to the edge of the single-crystal sample. The $Cu(111)$ surface was cleaned using cycles of Ar^+ sputtering followed by annealing in UHV at 720 K until no any impurities could be detected by XPS and a sharp (1×1) LEED pattern was observed.

The preparation recipe, adopted from Matolin et al.,[31] for the ceria films grown on a $Cu(111)$ substrate is described as follows. CeO_2 was grown in 2×10^{-7} Torr oxygen at a gradient substrate temperature. The oxygen background has been established for 2 min before starting Ce deposition. Ce was evaporated from a home-built tungsten basket. During the Ce deposition, the substrate temperature was initially kept at room temperature for 2 min and then increased to 790 K at a rate of approximately 3 K/s. After that, the sample was postannealed in oxygen at 790 K for 5 min. The oxygen background was kept until the sample was cooled down to 350 K. The coverage of CeO_2 was determined using Cu 2p signal attenuation in XPS, assuming the electron mean free path to be 1.12 nm in CeO_2 using Al $K\alpha$.[32] The monolayer of the ceria film is defined as a complete $CeO_2(111)$ layer with an O–Ce–O stack whose thickness is 0.31 nm.[33] In this study, ceria films with different thicknesses (0.4–5.0 nm) were grown separately and the thickness for each film was controlled by deposition time assuming a constant Ce deposition rate. Ceria films with different reduction degrees were obtained by two different methods. The slightly reduced thin film, $CeO_{2-x}(I)$, was obtained by vacuum annealing of the 2 nm thick fully oxidized CeO_2 thin film at 900 K for 30 min. While the strongly reduced 2 nm thick $CeO_{2-x}(II)$ thin film was obtained in a reduced oxygen pressure of 5×10^{-8} Torr.

Ag (99.999%, Alfa Aesar) was evaporated onto the ceria thin films at 300 K from a tantalum basket. The deposition rate of Ag was kept at ~0.1 monolayer (ML)/min. One ML of Ag is defined as the number of Ag atoms per area in a closed-packed layer (111) of bulk Ag atoms (1 ML = 1.4×10^{15} atoms/cm^2). The monolayer thickness is calculated to be 2.39 Å/ML. The coverage of Ag was calculated based on the mean particle volume and particle density of Ag on ceria, which were obtained from the STM studies, as described by Zhou et al.[10] However, owing to the tip convolution effects, the metal coverage might be overestimated. Therefore, during the STM measurement, great efforts were made to enhance the tip quality.

The STM images were collected at room temperature with a constant current mode (tunneling current: 0.01–0.05 nA; sample bias: 3–4 V) using an etched tungsten tip. The WSXM program[34] was used to process the STM images. The XPS spectra were collected at two different emission angles, 0° and 60° with respect to the surface normal, which provide relatively bulk sensitive and surface sensitive signals, respectively.

3. RESULTS

3.1. Ceria on Cu(111) with Different Thicknesses. In a previous STM study,[31] it was suggested that the growth of CeO_2 thin films on $Cu(111)$ proceeded in a Volmer–Weber mode. Ceria would not prefer to form a complete wetting layer on $Cu(111)$ due to the large lattice mismatch (~50%) between the ceria and the $Cu(111)$ substrate.[33,35] However, the morphology of ceria films can be adjusted by controlling the substrate temperature.[31] In order to obtain continuous CeO_2 thin films with large and flat terraces, we adopted the similar ceria growth procedure as reported in ref 31, but with additional postannealing, that is, the well-ordered CeO_2 thin
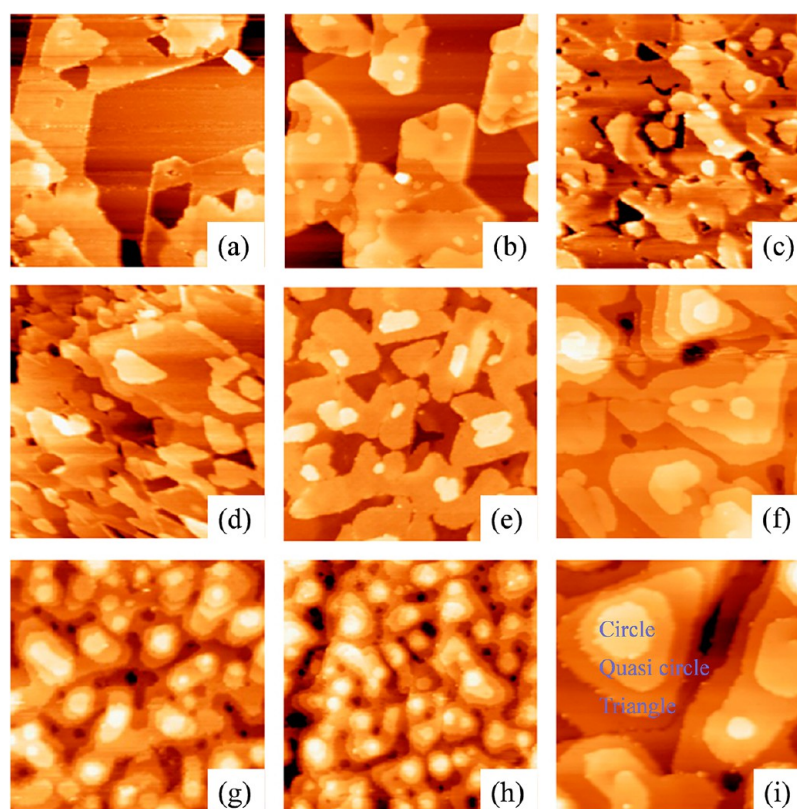
Figure 1. STM images (130 nm × 130 nm) of CeO$_2$ thin films of different thicknesses on Cu(111): 0.4 (a), 0.7 (b), 0.9 (c), 1.3 (d), 2.0 (e), 3.0 (f), 4.0 (g), and 5.0 nm (h). Image (65 nm × 65 nm) shown in (i) illustrates the different shapes of ceria terraces on 3.5 nm CeO$_2$ thin film. Images were taken with a constant current STM mode (3−4 V and 0.05−0.1 nA). Films shown in a−h were grown separately.

films were prepared by physical vapor deposition of Ce at room temperature in oxygen followed by increasing the substrate temperature to 790 K. Ceria films grown by this method have been demonstrated to be highly surface ordered with few open ceria monolayers.[31] Figure 1 presents a series of STM images of CeO$_2$ films with different thicknesses. As shown in Figure 1a,b, at low coverages of ceria (0.4 and 0.7 nm thick), 40−50% Cu surface is covered by ceria with tens of nanometers wide atomic flat terraces. Even at such low coverages, the second ceria layer starts to grow on the first layer. The step height between the neighboring terraces is measured to be 0.3 nm, in perfect agreement with the spacing of O−Ce−O trilayers in the bulk CeO$_2$(111) structure (0.31 nm).[33] At nominal coverage of 3 MLE (0.9 nm), ceria covers approximately 90% of the Cu surface (Figure 1c). The left 10% uncovered Cu surface is exposed as the dark holes, which have a height of almost 1 nm. When the ceria thickness increases to 1.3 nm, the Cu surface is fully covered with ceria. As shown in Figure 1d, the ceria films basically expose flat terraces with 3−4 open monolayers, which are separated by single O−Ce−O steps. At 2 nm, the ceria film become more continuous with less open monolayers which are organized in broad pyramids (Figure 1e).

With further increasing the thickness, the ceria thin film tends to grow three-dimensionally and becomes more and more discontinuous (Figure 1f−h). The size of the terraces decreases along with the increase of the number of open monolayers, causing the formation of many small ceria islands. The ceria islands have the diameter no more than ten nanometers, which can be recognized as the aggregate of CeO$_2$.[8] Correspondingly, the number of the step edges that have under-coordinated atoms increases. These step edges

could act as nucleation centers for silver particles, as seen later. It is interesting to note that the shape of the topmost ceria layers changes from triangle to circle when the ceria thickness is higher than 2 nm. This morphology change is demonstrated in Figure 1i, where from the view of top to bottom, the ceria layers with shapes of circle, quasi-circle and triangle on a 3.5 nm CeO$_2$ thin film can be clearly observed. In addition, a few of small CeO$_2$ nanoparticles are found on the step edges between terraces.

In previous studies of CeO$_2$/Cu(111) inverse model catalysts,[36−38] it has been reported that the existence of submonolayer ceria on Cu(111) facilitated the oxidation of the Cu substrate, leading to the formation of Cu$_2$O on the substrate surfaces near and underneath the ceria islands. In the present study, submonolayer ceria was grown on the Cu(111) surface. As shown in Figure 2a, the uncovered Cu(111) substrate surface shows paralleled line shape protrusions. Magnified STM image of this structure is displayed in Figure 2b, illustrating the "29" structure originated from the distortion of a Cu$_2$O(111) like layer.[39]

Figure 2c−e illustrates the LEED patterns of clean Cu(111), 2.0 and 4.0 nm thick CeO$_2$ thin films grown on Cu(111), respectively. It can be seen that after deposition of 2.0 nm thick CeO$_2$ thin film, the original hexagonal spots due to the Cu(111) substrate are significantly weakened. Instead, a group of extra hexagonal spots, corresponding to the (1.5 × 1.5) CeO$_2$(111)/Cu(111) structure, appears (Figure 2d). Further increasing the thickness of ceria thin film to 4.0 nm, the substrate spots completely disappear, only the spots of ceria are observed, as shown in Figure 2e. In addition, with the same background the spots from 4.0 nm thick ceria film are found to
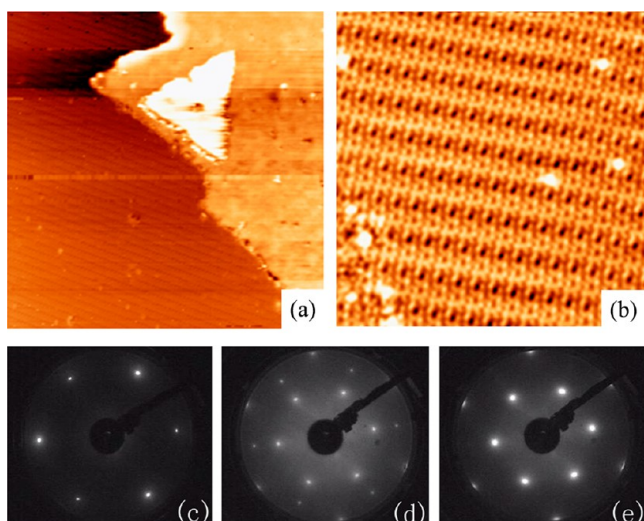
Figure 2. STM image of submonolayer of ceria on Cu(111) (a) and higher magnification of Cu_2O formed during the growth of ceria (b). Image size: 70 nm × 70 nm (a) and 30 nm × 30 nm (b). LEED pattern of the clean Cu(111) substrate (c), 2.0 nm CeO_2 thin film (d), and 4.0 nm CeO_2 thin film (e) are also shown. All LEED patterns were taken at 60 eV.

be not as sharp as those from the 2 nm thick CeO_2 film, implying that the ordering of CeO_2 thin film decreases with increasing the thickness of ceria film. This result is in good agreement with our STM study, where thicker CeO_2 films show rougher morphology in STM images, as shown in Figure 1.

3.2. Ceria of Different Stoichiometry on Cu(111).

In order to study the CeO_{2-x} films with different stoichiometry, two reduced ceria films with thicknesses of 2 nm, denoted as $CeO_{2-x}(I)$ and $CeO_{2-x}(II)$, were prepared. The former one was prepared by vacuum annealing of a 2 nm thick fully oxidized CeO_2 film at 1000 K for 30 min, while the latter one was produced by decreasing the oxygen pressure to 5×10^{-8} Torr during ceria growth. XPS data for the Ce 3d region of each CeO_{2-x} film collected with two different detecting angles with respect to the surface normal (θ) are displayed in Figure 3. As shown in the top spectrum of Figure 3a, which was taken at $\theta = 0°$ from the fully oxidized CeO_2 film, six peaks corresponding to three pairs of spin−orbit split doublets can be identified, which represent 4f configuration in the photoemission final state.[32] The spectra from the two reduced ceria films exhibit

two more pairs of doublets, which are originated from different Ce 4f configurations in both the initial and final states associated with Ce^{3+} ions.[10] The percentages of Ce^{4+} in the films were determined by fitting the Ce 3d XPS following the procedure introduced by Skala and co-workers.[40,41] Thus, the two reduced ceria thin films are calculated to be involved of 6 and 19% Ce^{3+}, corresponding to $CeO_{1.97}$ and $CeO_{1.91}$, respectively, at the detecting angle of 0°. It is clear that the nonstoichiometric ceria films obtained by vacuum annealing ($CeO_{2-x}(I)$) is only slightly reduced, while the ceria films produced by decreasing the oxygen pressure during growth ($CeO_{2-x}(II)$) is much more reduced. Moreover, when the detecting angle is alternated to 60° to make the spectra more surface sensitive, all three ceria films exhibit higher Ce^{3+} percentages within the detecting depth. As displayed in Figure 3b, the top curve of ceria film is calculated to contain 6% Ce^{3+}; this is reasonable since the detected concentration of surface defects and step edge sites that are consisted of under-coordinated Ce cations increase when the surface sensitivity increases. Most notably, compared to the spectrum collected at normal emission, the Ce^{3+} concentration in $CeO_{2-x}(I)$ significantly increases from 6% to 18% at $\theta = 60°$. Considering the detecting depth of spectra in Figure 3b is only half of that in Figure 3a, the different distributions of Ce^{3+} in $CeO_{2-x}(I)$ suggests that this ceria film is more reduced on the surface. In other words, oxygen vacancies mainly locate on the surface. This is plausible since the desorbing rate of oxygen from film to vacuum is higher at surface than it in the bulk during annealing. While in $CeO_{2-x}(II)$ the Ce^{3+} concentration increases from 19% to 40% at more surface sensitive detecting angle, suggesting that $CeO_{2-x}(II)$ films are largely reduced at both detecting angles. This means that there are substantial subsurface/bulk oxygen vacancies and surface oxygen vacancies in the $CeO_{2-x}(II)$ film. Our STM results can further distinguish the difference between these reduced ceria thin films.

Figure 4a−c present a series of STM images of CeO_2, $CeO_{2-x}(I)$ and $CeO_{2-x}(II)$ thin films. All the ceria films have large and flat terraces that fully cover the Cu(111) substrate. With increasing the degree of reduction, the density of surface defects increases and the ceria surface becomes rougher. This phenomenon can be better observed in Figure 4d−f (zoom out of Figure 4a−c, respectively). As it is generally known, the reduction of ceria films leads to the increase of the number of surface defects. On the surface of stoichiometric ceria, atomic resolution image of ceria film was observed (see the inset of
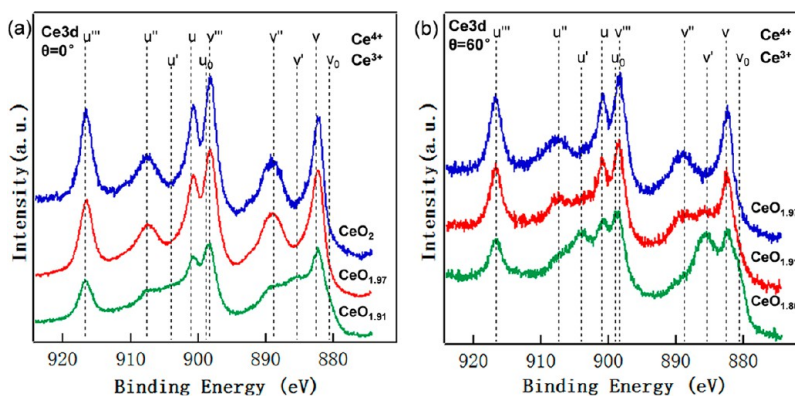
Figure 3. Ce 3d XPS spectra from three 2 nm-thick ceria thin films with different stoichiometry grown on Cu(111) collected at two different angles with respect to the surface normal: 0° (a) and 60° (b).
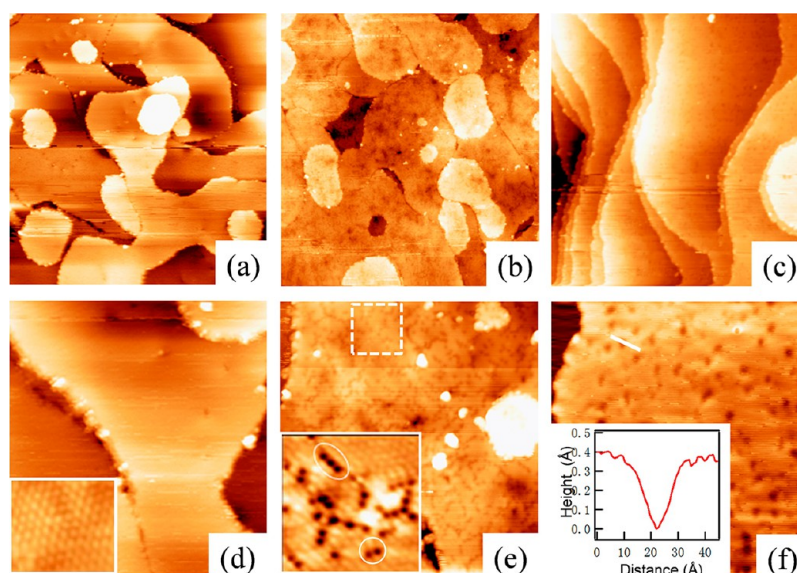
Figure 4. Large scale STM images (a−c) of 2 nm thick fully oxidized CeO_2 and two partially reduced ceria films ($CeO_{2−x}(I)$ and $CeO_{2−x}(II)$). (d−f) Magnified images of a, b, and c, respectively. The atomically resolved images measured on fully oxidized and slightly reduced ceria thin films are displayed in the inset of d and e, respectively; the linear oxygen vacancies dimer is labeled in circle while the linear oxygen vacancies trimer is labeled in oval. The inset of (f) shows the line scan profile of defect in (f). Image size: (a−c) 130 nm × 130 nm, (d−f) 39 nm × 39 nm, inset for (d): 3 nm × 3 nm, inset for (e): 5 nm × 5 nm.
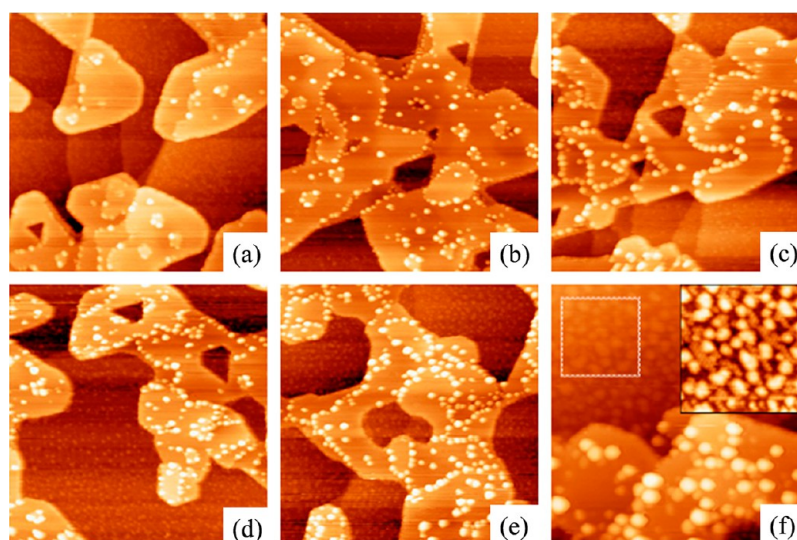
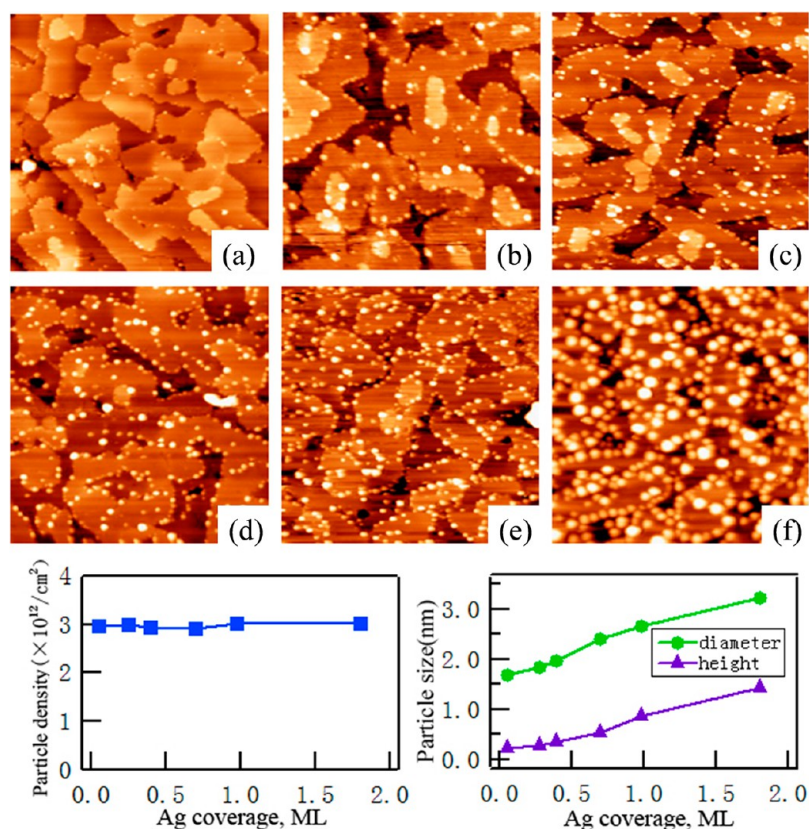
Figure 5. STM images of Ag deposited on 0.7 nm CeO_2 films with different coverages: 0.1 ML (a), 0.3 ML (b), 0.6 ML (c), 0.9 ML (d), 1.4 ML (e). Shown in (f) is the zoom out image of (e). The inset in (f) is the enlarged image of the square-marked area for Ag on copper. Image size: (a−e) 130 nm × 130 nm, (f) 65 nm × 65 nm, (inset) 20 nm × 20 nm. Note that the Ag coverages shown here were calculated based on Ag on ceria only.

Figure 4d). The measured distance between the two adjacent Ce atoms is 3.9 Å, which matches well with the 3.83 Å, the expected surface spacing.[42] For fully oxidized CeO_2 surface, the terrace step edges may contain under-coordinated Ce atoms, which are characteristic of Ce^{3+}. While on the $CeO_{2−x}(I)$ surface, except for the step edges, many defects on the terraces can be observed, which can be identified as single surface oxygen vacancies and their linear clusters, including dimers and trimmers, as marked in circle and oval, respectively in the inset of Figure 4e, which is the zoom out of the dashed square part of Figure 4e. Note that the surface oxygen vacancy linear clusters appear in three different orientations, reflecting the 3-fold symmetry of the $CeO_{2−x}(111)$ surface.[43] However, on the more reduced $CeO_{2−x}(II)$ surface, much larger defects on terraces

can be observed, as shown in Figure 4f. Although the atomic resolution image of these defects has not been obtained, it is not hard to find that these defects are mainly round with a mean diameter of ∼15 Å, as seen in the line scan profile in the inset of Figure 4f for a randomly selected defect. It is obvious that these defects are much larger than those on $CeO_{2−x}(I)$. Although the structure of these complicated surface defects cannot be distinguished by our STM result, these defects are suggested to be related with the oxygen vacancies, including surface and subsurface oxygen vacancies.[33,44,45] Removal of one oxygen on ceria surface results in the valence change $Ce^{4+} \rightarrow Ce^{3+}$ of two cations. Hence, the larger area of ceria film occupied by defects, the more reduced ceria films would be. These STM results agree very well with our XPS data,

Figure 6. STM images of Ag deposited on the 2 nm thick CeO_2 film with different Ag coverages: 0.05 ML (a), 0.3 ML (b), 0.4 ML (c), 0.7 ML (d), 1.0 ML (e), and 1.8 ML (f). Image size: 130×130 nm^2. The diagrams show particle density (left) and apparent size (right) as a function of silver coverage.

suggesting the increase of Ce^{3+} concentration in the ceria films from $CeO_{2-x}(I)$ to $CeO_{2-x}(II)$.

3.3. Ag Deposition on CeO_2 Thin Films at 300 K.
3.3.1. Ag Deposition on 0.7 nm CeO_2 Thin Films. The growth of Ag was first studied on 0.7 nm thick CeO_2 thin films to examine the effect of the Cu substrate and unfulfilled ceria film on the structural properties of Ag. Figure 5 illustrates the STM images of different coverages of Ag deposited on 0.7 nm thick ceria thin films at room temperature. At lowest Ag coverage studied, the Ag nanoparticles are mostly found on terrace step edges, demonstrating that interaction of silver with the ceria step edges is much stronger than with the regular terraces. Increase the Ag coverage results in the larger volume of particles at the terrace step edges (Figure 5b−e). At higher Ag coverages such as 1.0 ML, a few Ag nanoparticles can be found on ceria terraces.

It must be pointed out that the terrace step edges can be distinguished as two types, exhibiting distinct behaviors of Ag deposition. Ag nanoparticles exclusively decorate the terrace step edges between two different ceria layers, hereafter noted as ceria−ceria step edges. In contrast, no Ag particle can be found on the terrace step edges between the ceria layers with the copper substrate (noted as ceria-Cu step edges). Besides, it can be seen that the amount of Ag on copper substrate is larger than that on the ceria surface, especially at high coverage of Ag (Figure 5e,f). Specifically, the coverages of Ag on copper and ceria surface shown in Figure 5f can be quantified to be 2.2 and 1.4 ML, respectively. Based on the fact that the sticking probability of Ag onto ceria films is near unity,[16] we propose that Ag atoms initially deposited near the ceria-Cu step edges

diffuse from ceria surface to copper substrate through the ceria-Cu step, leading to the higher coverage of Ag on copper than on ceria.

3.3.2. Ag Deposition on 2 nm Fully Oxidized CeO_2 and Reduced CeO_{2-x} Thin Films. Figure 6 presents a series of STM images of Ag deposited onto the fully oxidized 2 nm thick $CeO_2(111)$ films at room temperature. Similar to Ag on the 0.7 nm CeO_2 film, the Ag adatoms mainly decorate the terrace step edges at low Ag coverages. Further increasing Ag coverage basically increases the particle size at nearly constant particle density, as can be seen from Figure 6a−f. Figure 6g,h summarize the data on the particle density and size as a function of Ag coverage. As displayed in Figure 6g, the Ag particle density keeps almost constant at $\sim 3 \times 10^{12}$ /cm^2 during Ag growth. The aspect ratio is ~ 0.2, which indicates a hemispherical cap shape of deposited Ag nanoparticles.[16] These results agree well with our previous study,[18] suggesting a three-dimensional growth mode of Ag on CeO_2 thin films. Note that the number of Ag particle density reported here is slightly lower than that reported by Farmer et al. estimated from low energy ion scattering (LEIS) and Auger electron spectroscopy (AES; 4×10^{12}/cm^2) for Ag growth on 4 nm thick $CeO_{2-x}(111)$ ($x = \sim 0.1$) thin films.[16] This is reasonable since the ceria film thickness studied here (2 nm) is thinner and the number of defects including steps and kinks for Ag particle growth is lower than that on 4 nm thick films, as observed in Figure 1.

The influence of surface defects on Ag growth is also studied by depositing same amount of Ag onto two reduced ($CeO_{2-x}(I)$ and $CeO_{2-x}(II)$) ceria thin films. Surprisingly, there is no obvious difference between Ag on CeO_2 and Ag on
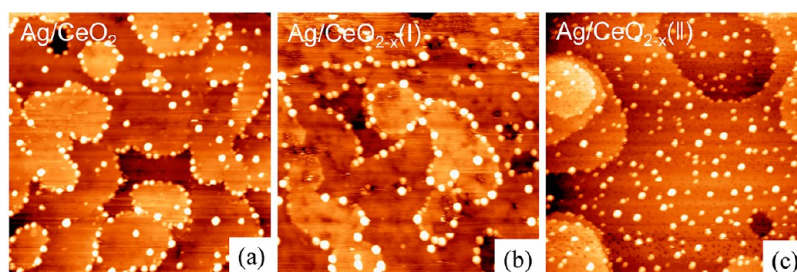
Figure 7. STM images of 0.7 ML Ag deposited on (a) CeO_2; (b) $CeO_{2-x}(I)$ obtained by UHV annealing of CeO_2 for 30 min; (c) $CeO_{2-x}(II)$ prepared by depositing Ce in the reduced oxygen pressure of 5×10^{-8} Torr. Image size: 130 nm × 130 nm for all.

$CeO_{2-x}(I)$ (Figure 7a,b). The particle densities of Ag particles are almost identical on both CeO_2 and $CeO_{2-x}(I)$, which implies that single surface oxygen vacancy and even their linear agglomerates do not act as the nucleation centers for Ag particle growth. On CeO_2 and $CeO_{2-x}(I)$, a few Ag particles can be found anchored on terraces, which are probably bonded to small CeO_2 step edges or larger defects such as holes instead of point defects. This phenomenon is further evidenced on $CeO_{2-x}(II)$ film. As displayed in Figure 7c, Ag particles randomly distribute on both terraces and step edges. As mentioned above, with the highest reduction degree in this study, this $CeO_{2-x}(II)$ film exhibits a lot of large and circular holes on terraces, which are related to the missing of surface and subsurface oxygen atoms. Because of the presence of these large defects, Ag nanoparticles are dispersed on ceria terraces with a higher particle density and smaller particle size on the $CeO_{2-x}(II)$ surface.

3.4. Thermal Sintering. The sintering behavior of Ag is also studied by subsequently annealing the Ag nanoparticles formed on the 2 nm thick stoichiometric (CeO_2) and slightly reduced ceria $(CeO_{2-x}(I))$ films at 300 K to elevated temperatures of 500, 660, and 800 K (Figure 8). On CeO_2, Ag nanoparticles show no preference of aggregation up to 500 K. The particle density remains $3 \times 10^{12}/cm^2$. Subsequent annealing of this surface to 660 K results in the significant decrease of the number of particle density and the increase of sizes of the Ag particles, suggesting that Ag nanoparticles undergo sintering upon annealing. Moreover, calculated by multiplying the mean particle volume by particle density, the total amount of Ag adatoms does not decrease compared to the initial Ag deposition at 300 K, indicating that Ag desorption from CeO_2 surface does not occur at 660 K. Further annealing to 800 K leads to a continuous increase in particle size, accompanied by a significant decrease of particle density and total Ag amount, implying that Ag nanoparticles experience both sintering and desorption processes at 800 K. Note that the possibility of Ag diffusion into the $CeO_2(111)$ substrate upon annealing can be ruled out.[18] This STM observation of the sintering behavior of Ag on CeO_2 is consistent with our previous study.[18]

As can be been in Figure 8b, the growth behavior of Ag show unobservable difference on $CeO_{2-x}(I)$ compared to CeO_2 at 300 K. Moreover, the Ag thermal behaviors on these two ceria films are observed to be almost same upon heating to 500 K. However, although the sintering of Ag on $CeO_{2-x}(I)$ (Figure 8f) is also observed at 660 K, the particle density is much higher and the particle size is much smaller than those on CeO_2 at the same temperature (Figure 8e), suggesting that the sintering process of Ag particles is slower on the reduced surface. Further annealing to 800 K results in both sintering and desorption of
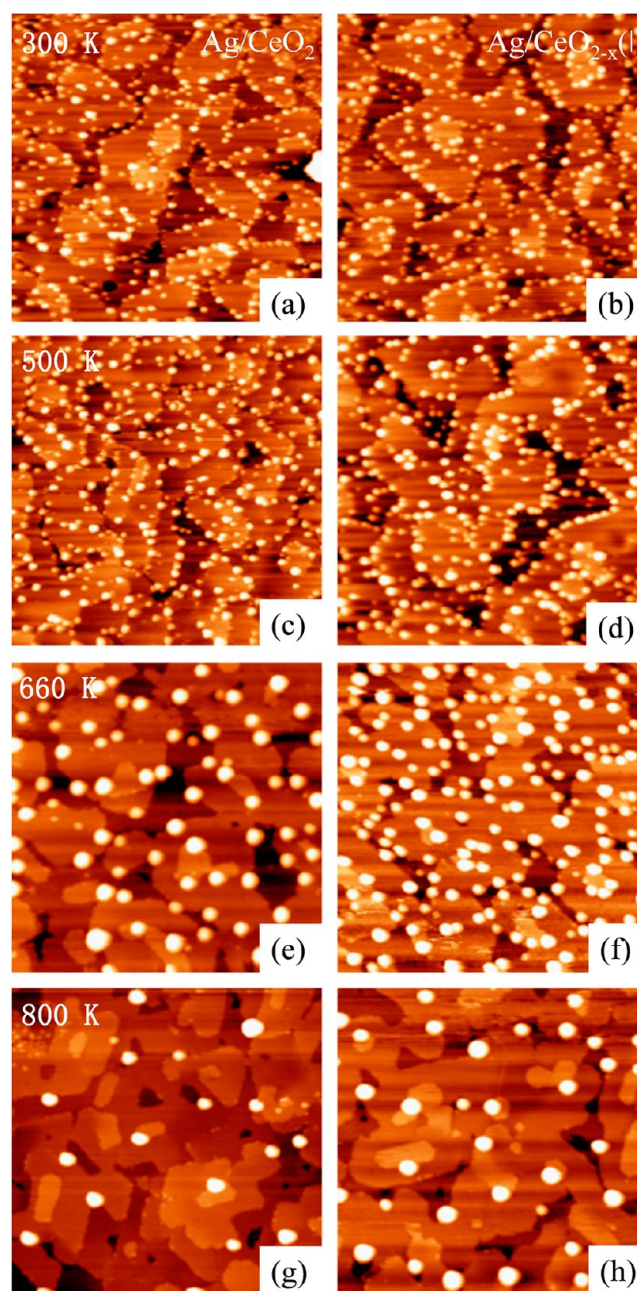
Figure 8. STM images of 2 nm-thick CeO_2 (a) and $CeO_{2-x}(I)$ (b) films upon 1.0 ML of Ag deposited at 300 K and then subsequently anneal to 500 K (c, d), 660 K (e, f), and 800 K (g, h), respectively. Image sizes are 130 nm × 130 nm.

Ag nanoparticles on $CeO_{2-x}(I)$. But the amount of Ag remained on the $CeO_{2-x}(I)$ surface is larger than that on CeO_2 at the sample temperature, indicating less desorption of Ag on $CeO_{2-x}(I)$. Moreover, Ag particles on strongly reduced ceria films exhibit slower sintering process and higher desorption temperature compared to those on slightly reduced ceria films with the same initial Ag coverage (see Figure S1 in Supporting Information), implying that an increase in the reduction degree of ceria films leads to higher thermal stability of Ag nanoparticles. This result is similar to other transient metals on reduced CeO_2 films upon annealing.[10,46,47]

4. DISCUSSION

4.1. Influence of Surface Defects on Ag Growth and Sintering.

Our results suggest that on the slightly reduced ceria surface which was obtained by vacuum annealing the stoichiometric CeO_2, single oxygen vacancy and their linear clusters appearing as dimers and trimmers mainly locate on the surface. It seems that these oxygen vacancies do not act as nucleation centers for Ag nanoparticle growth, although DFT calculations have demonstrated that Ag exhibits stronger interaction with oxygen vacancies than with regular CeO_2 surface.[15] Compared to the step edge sites, the interaction of Ag with these surface oxygen vacancies is relatively weaker because most of Ag particles still nucleate at the step edges in the presence of these oxygen vacancies, as observed in Figure 7b. However, on the strongly reduced ceria surface prepared by depositing Ag in the reduced oxygen pressure, much large defects which are related to surface and subsurface oxygen vacancies appear on the terrace of the ceria film. These defects can act as nucleation centers for Ag growth (Figure 7c), suggesting that the interaction of Ag with large surface and subsurface oxygen vacancies is much stronger than that of Ag with the small surface oxygen vacancies (single, dimer and linear trimmer oxygen vacancies). This observation is consistent with what proposed by Campbell et al. that the subsurface oxygen vacancies can increase the bonding of Ag to the ceria surface.[48] In addition, these results also suggest that the reduction degree of ceria strongly influence the Ag growth. Theoretical studies of Au nanoclusters (NCs) performed by Henkelman et al.[49,50] showed that the binding energy (hereafter denoted as E_{bind}) of Au NCs supported on stoichiometric CeO_2 surface is 3.15 eV. While the E_{bind} of Au NCs on CeO_2 with 13% Ce^{3+} and CeO_2 with 19% Ce^{3+} are 3.78 and 4.11 eV, respectively. Moreover, the E_{bind} of Au NCs supported on CeO_2 step is 3.96 eV. Hence, the sequence of E_{bind} can be listed as follow: $Au/CeO_{1.90} > Au/CeO_2$ step edge $> Au/CeO_{1.93} > Au/$ regular CeO_2.[49] These results indicate that one can only observe Au NCs populating on the terrace sites when the reduction degree reaches a certain level. Considering the similar adsorption property of Ag on CeO_2 compared with Au,[51] these theoretical results agree well with our present results.

Our results show that although the surface oxygen vacancies on the slightly reduced ceria film cannot anchor Ag particles during their growth, they do affect the sintering behavior of Ag nanoparticles. The STM results clearly illustrate that the sintering process of Ag on slightly reduced ceria film is slower than that of Ag on fully oxidized CeO_2 film at the same temperature. This means that although the interaction between Ag nanoparticles and the surface oxygen vacancies is weaker than that of Ag with step edges, it is still stronger than the interaction of Ag with perfect CeO_2 terrace sites. Thus, during the thermal annealing, the diffusion of Ag particles across the terrace is slowed down once they meet the surface oxygen vacancies. However, since the overall interaction of Ag with surface oxygen vacancies is still too weak to completely hinder the diffusion of Ag on ceria, thus the sintering process of Ag nanoparticles can still happen, but occurs at slightly higher temperature than on the fully oxidized CeO_2 film. Moreover, with increasing the reduction degree of ceria films, the interaction between surface defects and Ag becomes stronger, the Ag sintering process gets even slower. The enhanced thermal stability of metal particles on reduced ceria film can be also found on similar systems such as Pd, Rh, and Pt on CeO_2.[10,11]

4.2. Mechanism of Reduction of Ceria Film.

Many studies have reported that the reduction of ceria was observed upon the deposition of metals such as Pd,[52] Pt,[9,53] Au,[54] and Ag[15,18] on ceria. However, the mechanism of metal-induced reduction of the CeO_2 films is still under debate.[52,54−57] Regarding the present Ag/CeO_2 system, despite that a lot of effects have been made to investigate the mechanism of Ag-induced reduction of CeO_2 films, there is no certain conclusively explanation for this phenomenon. In our previous study,[18] we observed the Ag-induced ceria reduction. By using the Auger parameter method, we differentiated the contributions of initial- and final-state effects of the Ag 3d binding energy (BE) shifts toward a higher BE at low coverages with respect to the bulk value. We found that the initial-state effect contribution was negligible, and concluded that Ag maintained metallic state during the growth on ceria. Thus, we attributed the possible reason for the Ag-induced reduction of $CeO_2(111)$ to the spillover of lattice oxygen in CeO_2 at the Ag/CeO_2 boundary to the surface of the supported Ag nanoparticles. However, Luches et al.[15] reported that the oxygen reverse spillover could not occur at the Ag/CeO_2 boundary according to their theoretical calculation.[58] They found that the cost of moving one O atom from the ceria surface to the adsorbed Ag nanoparticles was too high, which made the oxygen reverse spillover from the $CeO_2(111)$ surface to Ag energetically unfavorable. Thus, they concluded that the reduction of ceria was caused by the charge transfer from Ag to ceria. It should be mentioned that these calculations was carried out for Ag on the $CeO_2(111)$ regular surface.[15,58]

However, our STM results demonstrate that Ag mainly populates the step edges of the $CeO_2(111)$ surface, no matter how thick the film is. It is hard to find Ag particles on the regular $CeO_2(111)$ surface. Therefore, the calculation based on Ag on regular $CeO_2(111)$ surface seems to be not appropriate. In fact, several recent studies[29,49,59,60] reported a completely different picture for nanostructured ceria including ceria nano islands and step edges of ceria from the regular bulk $CeO_2(111)$. It was found that the rate-limit-step of the oxygen reverse spillover is the formation of oxygen vacancies.[15] The cost to create an oxygen vacancy, hereafter denoted as E_{vac}, is 2.25 eV for regular $CeO_2(111)$ slap, if calculated with respect to half of O_2 molecular.[15] While decreasing the size of ceria crystallites to the nanoscale, a much smaller E_{vac} was obtained, mainly due to the quantum size effect. Take the $Ce_{40}O_{80}$ particle for example, the E_{vac} is 0.80 eV.[29] Similarly, the E_{vac} value on the steps was calculated to be up to 0.7 eV lower than on a regular $CeO_2(111)$ surface.[60] Moreover, for a nanoscale system consisting of a Pt_8 cluster on a stoichiometric $Ce_{40}O_{80}$ support, the energy for oxygen reverse spillover is −0.51 eV, which is completely different from the 1.0 eV found for the $Pt_8/CeO_2(111)$ system. This result suggests that the migration of

oxygen from ceria with nanoscale size to Pt nanoparticles is an energetically favorable process, accompanied by the reduction of two Ce^{4+} to Ce^{3+}.

Our previous study of $Ag/CeO_2(111)$ was carried out on a 4.0 nm thick CeO_2 film.[18] As revealed by the present STM observation, this 4 nm ceria film is relatively more discontinuous and less ordering, exhibiting a large number of small ceria islands on the topmost layer. These islands are actually small aggregates of CeO_2, similar to the ceria thin films prepared by Libuda et al.[8] With a high particle density, the Ag nanoparticles on this film remain small in size even at the high coverages. Therefore, it is expected that the energy cost for the reverse spillover of oxygen on these nanostructured CeO_2 to the nearby small Ag particles should be much lower than that on the regular $CeO_2(111)$ surface, making this process possibly happen for the system of Ag nanoparticles on ceria thin films.

Note that except for the oxygen reverse spillover mechanism, the reduction of ceria film could also be possibly attributed to the Ag-induced segregation of subsurface oxygen vacancies to surface, as proposed by Campbell et al. recently.[48] These subsurface oxygen vacancies could be attracted from deeper in ceria up to the bottom of Ag islands on-top to stabilize the Ag/ceria bonding, leading to the increase the Ce^{3+} concentration observed in the XPS signals.[18] From our current data, it is not possible to determine which of these two mechanisms is more appropriate since both of these mechanisms can explain no measurable loss of electron density from the Ag.[18] Therefore, further theoretical study is needed to confirm which mechanism is more reasonable.

5. CONCLUSION

Our STM results of CeO_2 thin films with different thicknesses suggest the morphology of the films is strongly dependent on the coverage of ceria. With increasing the thickness, the ceria thin films become more discontinuous and defective, accompanied by the increasing of step edge sites. Ag grows three-dimensionally on the ceria films. On the stoichiometric $CeO_2(111)$ surface, Ag mainly nucleates at the step edge sites, independent of the film thickness. On the lightly reduced ceria surface, single surface oxygen vacancies and their linear agglomerates do not anchor Ag particles during Ag deposition at 300 K, but inhibit Ag from sintering and desorbing on ceria films upon vacuum annealing. While on the strongly reduced ceria films, the large defect sites can anchor the Ag particles, leading to the population of Ag particles on terrace sites. All these results suggest that Ag mainly grows on the nanoscale ceria, including the ceria step edge sites and small ceria islands, providing a possible pathway for oxygen reverse spillover from Ag/CeO_2 boundary to supported Ag nanoparticles.

ASSOCIATED CONTENT

S **Supporting Information**

Additional information is presented in Figure S1. This material is available free of charge via the Internet at http://pubs.acs.org.

AUTHOR INFORMATION

Corresponding Author

*E-mail: jfzhu@ustc.edu.cn.

Notes

The authors declare no competing financial interest.

ACKNOWLEDGMENTS

REFERENCES

(1) Kaspar, J.; Fornasiero, P.; Graziani, M. Use of CeO_2-Based Oxides in the Three-Way Catalysis. *Catal. Today* **1999**, *50*, 285−298.

(2) Avgouropoulos, G.; Ioannides, T.; Matralis, H. K.; Batista, J.; Hocevar, S. CuO−CeO₂ Mixed Oxide Catalysts for the Selective Oxidation of Carbon Monoxide in Excess Hydrogen. *Catal. Lett.* **2001**, *73*, 33−40.

(3) Bunluesin, T.; Gorte, R. J.; Graham, G. W. Studies of the Water-Gas-Shift Reaction on Ceria-Supported Pt, Pd, and Rh: Implications for Oxygen-Storage Properties. *Appl. Catal. B: Environ.* **1998**, *15*, 107−114.

(4) Deluga, G. A.; Salge, J. R.; Schmidt, L. D.; Verykios, X. E. Renewable Hydrogen from Ethanol by Autothermal Reforming. *Science* **2004**, *303*, 993−997.

(5) Fu, Q.; Weber, A.; Flytzani-Stephanopoulos, M. Nanostructured Au-CeO₂ Catalysts for Low-Temperature Water-Gas Shift. *Catal. Lett.* **2001**, *77*, 87−95.

(6) Farrauto, R.; Hwang, S.; Shore, L.; Ruettinger, W.; Lampert, J.; Giroux, T.; Liu, Y.; Ilinich, O. New Material Needs for Hydrocarbon Fuel Processing: Generating Hydrogen for the PEM Fuel Cell. *Annu. Rev. Mater. Res.* **2003**, *33*, 1−27.

(7) Norenberg, H.; Briggs, G. A. D. Defect Structure of Non-stoichiometric $CeO_2(111)$ Surfaces Studied by Scanning Tunneling Microscopy. *Phys. Rev. Lett.* **1997**, *79*, 4222−4225.

(8) Lykhach, Y.; Staudt, T.; Lorenz, M. P. A.; Streber, R.; Bayer, A.; Steinruck, H. P.; Libuda, J. Microscopic Insights into Methane Activation and Related Processes on Pt/Ceria Model Catalysts. *ChemPhysChem* **2010**, *11*, 1496−1504.

(9) Matolin, V.; Johanek, V.; Skoda, M.; Tsud, N.; Prince, K. C.; Skala, T.; Matolinova, I. Methanol Adsorption and Decomposition on Pt/CeO₂(111)/Cu(111) Thin Film Model Catalyst. *Langmuir* **2010**, *26*, 13333−13341.

(10) Zhou, Y. H.; Perket, J. M.; Zhou, J. Growth of Pt Nanoparticles on Reducible $CeO_2(111)$ Thin Films: Effect of Nanostructures and Redox Properties of Ceria. *J. Phys. Chem. C* **2010**, *114*, 11853−11860.

(11) Zhou, J.; Baddorf, A. P.; Mullins, D. R.; Overbury, S. H. Growth and Characterization of Rh and Pd Nanoparticles on Oxidized and Reduced $CeO_x(111)$ Thin Films by Scanning Tunneling Microscopy. *J. Phys. Chem. C* **2008**, *112*, 9336−9345.

(12) Trovarelli, A.; de Leitenburg, C.; Boaro, M.; Dolcetti, G. The Utilization of Ceria in Industrial Catalysis. *Catal. Today* **1999**, *50*, 353−367.

(13) Szabova, L.; Camellone, M. F.; Huang, M.; Matolin, V.; Fabris, S. Thermodynamic, Electronic and Structural Properties of Cu/CeO_2 Surfaces and Interfaces from First-Principles DFT+U Calculations. *J. Chem. Phys.* **2010**, *133*, 234705.

(14) Kong, D. D.; Pan, Y. H.; Wang, G. D.; Pan, H. B.; Zhu, J. F. Growth and Electronic Properties of Ag Nanoparticles on Reduced $CeO_{2−x}(111)$ Films. *Chin. J. Chem. Phys.* **2012**, *25*, 713−718.

(15) Luches, P.; Paglaica, F.; Valeri, S.; Preda, G.; Pacchioni, G. Nature of Ag Islands and Nanoparticles on the $CeO_2(111)$ Surface. *J. Phys. Chem. C* **2012**, *116*, 1122−1132.

(16) Farmer, J. A.; Baricuatro, J. H.; Campbell, C. T. Ag Adsorption on Reduced $CeO_2(111)$ Thin Films. *J. Phys. Chem. C* **2010**, *114*, 17166−17172.

(17) Farmer, J. A.; Campbell, C. T. Ceria Maintains Smaller Metal Catalyst Particles by Strong Metal-Support Bonding. *Science* **2010**, *329*, 933−936.

(18) Kong, D. D.; Wang, G. D.; Pan, Y. H.; Hu, S. W.; Hou, J. B.; Pan, H. B.; Campbell, C. T.; Zhu, J. F. Growth, Structure, and Stability of Ag on CeO$_2$(111): Synchrotron Radiation Photoemission Studies. *J. Phys. Chem. C* **2011**, *115*, 6715−6725.

(19) Akita, T.; Tanaka, K.; Kohyama, M. TEM and HAADF-STEM Study of the Structure of Au Nano-Particles on CeO$_2$. *J. Mater. Sci.* **2008**, *43*, 3917−3922.

(20) Weststrate, C. J.; Resta, A.; Westerstrom, R.; Lundgren, E.; Mikkelsen, A.; Andersen, J. N. CO Adsorption on a Au/CeO$_2$ (111) Model Catalyst. *J. Phys. Chem. C* **2008**, *112*, 6900−6906.

(21) Weststrate, C. J.; Westerstrom, R.; Lundgren, E.; Mikkelsen, A.; Andersen, J. N. Influence of Oxygen Vacancies on the Properties of Ceria-Supported Gold. *J. Phys. Chem. C* **2009**, *113*, 724−728.

(22) Zhou, Y. H.; Perket, J. M.; Crooks, A. B.; Zhou, J. Effect of Ceria Support on the Structure of Ni Nanoparticles. *J. Phys. Chem. Lett.* **2010**, *1*, 1447−1453.

(23) Zhou, Y.; Zhou, J. Interactions of Ni Nanoparticles with Reducible CeO$_2$(111) Thin Films. *J. Phys. Chem. C* **2012**, 9544−9549.

(24) Schwartz, J. M.; Schmidt, L. D. Microstructures of Pt-Ce and Rh-Ce Particles on Alumina and Silica. *J. Catal.* **1992**, *138*, 283−293.

(25) Kalakkad, D.; Datye, A. K.; Robota, H. Interaction of Platinum and Ceria Probed by Transmission Electron-Microscopy and Catalytic Reactivity. *Appl. Catal. B: Environ.* **1992**, *1*, 191−219.

(26) Kundakovic, L.; Flytzani-Stephanopoulos, M. Cu and Ag Modified Cerium Oxide Catalysts for Methane Oxidation. *J. Catal.* **1998**, *179*, 203−221.

(27) Bera, P.; Patil, K. C.; Hegde, M. S. NO Reduction, CO and Hydrocarbon Oxidation Over Combustion Synthesized Ag/CeO$_2$ Catalyst. *Phys. Chem. Chem. Phys.* **2000**, *2*, 3715−3719.

(28) Wagner, C. D. Auger Lines in X-ray Photoelectron Spectrometry. *Anal. Chem.* **1972**, *44*, 967−973.

(29) Vayssilov, G. N.; Lykhach, Y.; Migani, A.; Staudt, T.; Petrova, G. P.; Tsud, N.; Skala, T.; Bruix, A.; Illas, F.; Prince, K. C.; et al. Support Nanostructure Boosts Oxygen Transfer to Catalytically Active Platinum Nanoparticles. *Nat. Mater.* **2011**, *10*, 310−315.

(30) Xu, Q.; Hu, S. W.; Cheng, D. L.; Feng, X. F.; Han, Y.; Zhu, J. F. Growth and Electronic Structure of Sm on Thin Al$_2$O$_3$/Ni$_3$Al(111) Films. *J. Chem. Phys.* **2012**, *136*, 154705.

(31) Dvorak, F.; Stetsovych, O.; Steger, M.; Cherradi, E.; Matolinova, I.; Tsud, N.; Skoda, M.; Skala, T.; Myslivecek, J.; Matolin, V. Adjusting Morphology and Surface Reduction of CeO$_2$(111) Thin Films on Cu(111). *J. Phys. Chem. C* **2011**, *115*, 7496−7503.

(32) Sutara, F.; Cabala, M.; Sedlacek, L.; Skala, T.; Skoda, M.; Matolin, V.; Prince, K. C.; Chab, V. Epitaxial Growth of Continuous CeO$_2$(111) Ultra-Thin Films on Cu(111). *Thin Solid Films* **2008**, *516*, 6120−6124.

(33) Lu, J. L.; Gao, H. J.; Shaikhutdinov, S.; Freund, H. J. Morphology and Defect Structure of the CeO$_2$(111) Films Grown on Ru(0001) as Studied by Scanning Tunneling Microscopy. *Surf. Sci.* **2006**, *600*, 5004−5010.

(34) Horcas, I.; Fernandez, R.; Gomez-Rodriguez, J. M.; Colchero, J.; Gomez-Herrero, J.; Baro, A. M. WSXM: A Software for Scanning Probe Microscopy and a Tool for Nanotechnology. *Rev. Sci. Instrum.* **2007**, *78*, 013705.

(35) Luches, P.; Pagliuca, F.; Valeri, S. Morphology, Stoichiometry, and Interface Structure of CeO$_2$ Ultrathin Films on Pt(111). *J. Phys. Chem. C* **2011**, *115*, 10718−10726.

(36) Wrobel, R.; Suchorski, Y.; Becker, S.; Weiss, H. Cerium Oxide Layers on the Cu(111) Surface: Substrate-Mediated Redox Properties. *Surf. Sci.* **2008**, *602*, 436−442.

(37) Rodriguez, J. A.; Graciani, J.; Evans, J.; Park, J. B.; Yang, F.; Stacchiola, D.; Senanayake, S. D.; Ma, S. G.; Perez, M.; Liu, P.; et al. Water-Gas Shift Reaction on a Highly Active Inverse CeO$_x$/Cu(111) Catalyst: Unique Role of Ceria Nanoparticles. *Angew. Chem., Int. Ed.* **2009**, *48*, 8047−8050.

(38) Yang, F.; Graciani, J.; Evans, J.; Liu, P.; Hrbek, J.; Sanz, J. F.; Rodriguez, J. A. CO Oxidation on Inverse CeO$_x$/Cu(111) Catalysts: High Catalytic Activity and Ceria-Promoted Dissociation of O$_2$. *J. Am. Chem. Soc.* **2011**, *133*, 3444−3451.

(39) Matsumoto, T.; Bennett, R. A.; Stone, P.; Yamada, T.; Domen, K.; Bowker, M. Scanning Tunneling Microscopy Studies of Oxygen Adsorption on Cu(111). *Surf. Sci.* **2001**, *471*, 225−245.

(40) Skala, T.; Sutara, F.; Skoda, M.; Prince, K. C.; Matolin, V. Palladium Interaction with CeO$_2$, Sn-Ce-O, and Ga-Ce-O Layers. *J. Phys.: Condens. Matter* **2009**, *21*, 055005.

(41) Skala, T.; Sutara, F.; Prince, K. C.; Matolin, V. Cerium Oxide Stoichiometry Alteration via Sn Deposition: Influence of Temperature. *J. Electron Spectrosc. Relat. Phenom.* **2009**, *169*, 20−25.

(42) Fukui, K.; Namai, Y.; Iwasawa, Y. Imaging of Surface Oxygen Atoms and Their Defect Structures on CeO$_2$(111) by Noncontact Atomic Force Microscopy. *Appl. Surf. Sci.* **2002**, *188*, 252−256.

(43) Esch, F.; Fabris, S.; Zhou, L.; Montini, T.; Africh, C.; Fornasiero, P.; Comelli, G.; Rosei, R. Electron Localization Determines Defect Formation on Ceria Substrates. *Science* **2005**, *309*, 752−755.

(44) Zhang, C.; Michaelides, A.; King, D. A.; Jenkins, S. J. Oxygen Vacancy Clusters on Ceria: Decisive Role of Cerium Electrons. *Phys. Rev. B* **2009**, *79*, 075433.

(45) Henderson, M. A.; Perkins, C. L.; Engelhard, M. H.; Thevuthasan, S.; Peden, C. H. F. Redox Properties of Water on the Oxidized and Reduced Surfaces of CeO$_2$(111). *Surf. Sci.* **2003**, *526*, 1−18.

(46) Zhou, J.; Baddorf, A. P.; Mullins, D. R.; Overbury, S. H. Growth and Characterization of Rh and Pd Nanoparticles on Oxidized and Reduced CeO$_x$(111) Thin Films by Scanning Tunneling Microscopy. *J. Phys. Chem. C* **2008**, *112*, 9336−9345.

(47) Lu, J. L.; Gao, H. J.; Shaikhutdinov, S.; Freund, H. J. Gold Supported on Well-Ordered Ceria Films: Nucleation, Growth and Morphology in CO Oxidation Reaction. *Catal. Lett.* **2007**, *114*, 8−16.

(48) Campbell, C. T.; Sellers, J. R. Anchored Metal Nanoparticles: Effects of Support and Size on Their Energy, Sintering Resistance and Reactivity. *Faraday Discuss.* **2013**, *162*, 9−30.

(49) Kim, H. Y.; Henkelman, G. CO Oxidation at the Interface of Au Nanoclusters and the Stepped-CeO$_2$(111) Surface by the Mars−Van Krevelen Mechanism. *J. Phys. Chem. Lett.* **2012**, *4*, 216−221.

(50) Kim, H. Y.; Lee, H. M.; Henkelman, G. CO Oxidation Mechanism on CeO$_2$ Supported Au Nanoparticles. *J. Am. Chem. Soc.* **2011**, *134*, 1560−1570.

(51) Piotrowski, M. J.; Tereshchuk, P.; Da Silva, J. L. F. Theoretical Investigation of Small Transition-Metal Clusters Supported on the CeO$_2$(111) Surface. *J. Phys. Chem. C* **2014**, *118*, 21438−21446.

(52) Wilson, E. L.; Chen, Q.; Brown, W. A.; Thornton, G. CO Adsorption on the Model Catalyst Pd/CeO$_{2-x}$(111)/Rh(111). *J. Phys. Chem. C* **2007**, *111*, 14215−14222.

(53) Mullins, D. R.; Zhang, K. Z. Metal-Support Interactions Between Pt and Thin Film Cerium Oxide. *Surf. Sci.* **2002**, *513*, 163−173.

(54) Skoda, M.; Cabala, M.; Matolinova, I.; Prince, K. C.; Skala, T.; Sutara, F.; Veltruska, K.; Matolin, V. Interaction of Au with CeO$_2$(111): A Photoemission Study. *J. Chem. Phys.* **2009**, *130*, 034703.

(55) Wilson, E. L.; Grau-Crespo, R.; Pang, C. L.; Cabailh, G.; Chen, Q.; Purton, J. A.; Catlow, C. R. A.; Brown, W. A.; de Leeuw, N. H.; Thornton, G. Redox Behavior of the Model Catalyst Pd/CeO$_{2-x}$/Pt(111). *J. Phys. Chem. C* **2008**, *112*, 10918−10922.

(56) Smirnov, M. Y.; Graham, G. W. Pd Oxidation Under UHV in a Model Pd/ceria−Zirconia Catalyst. *Catal. Lett.* **2001**, *72*, 39−44.

(57) Valdimir Shapovalov; Metiu, H. Catalysis by Doped Oxides: CO Oxidation by Au$_x$Ce$_{1-x}$O$_2$. *J. Catal.* **2007**, *245*, 205−214.

(58) Preda, G.; Pacchioni, G. Formation of Oxygen Active Species in Ag-Modified CeO$_2$ Catalyst for Soot Oxidation: A DFT Study. *Catal. Today* **2011**, *177*, 31−38.

(59) Migani, A.; Vayssilov, G. N.; Bromley, S. T.; Illas, F.; Neyman, K. M. Greatly Facilitated Oxygen Vacancy Formation in Ceria Nanocrystallites. *Chem. Commun.* **2010**, *46*, 5936−5938.

(60) Kozlov, S. M.; Neyman, K. M. O Vacancies on Steps on the CeO$_2$(111) Surface. *Phys. Chem. Chem. Phys.* **2014**, *16*, 7823−7829.